Axel's analysis of Etienne's data

http://norlx51.nordita.org/~brandenb/issi/etienne/

October 24, 2019, Revision: 1.32

We analyze the magnetic energy and helicity spectra for the simulations of Etienne of erupting and nonerupting regions, as described by Leake et al. (2014). The spectra are normalized such that

$$\tfrac{1}{2}\langle \boldsymbol{B}^2 \rangle \equiv \mathcal{E}_{\rm M} = \int E_{\rm M}(k)\,{\rm d}k, \tag{1}$$

$$\langle A_z B_z \rangle \equiv \mathcal{H}_{\rm M} = \int H_{\rm M}(k)\,{\rm d}k, \tag{2}$$

and $\nabla^2 A_z = -J_z$ in the Coulomb gauge. We determine these spectra on the lower boundary of the simulation domain at the three times provided ($t = 140$, 280, and 320). We see that the magnetic helicity has positive values at all wavenumbers below $kL_0 = 1$. At later times, the peak of the fractional magnetic helicity moves to progressively smaller wavenumbers, down to about 0.3–0.4, and the fractional magnetic helicity decreases. It is useful to define

$$r(k) = kH_{\rm M}(k)/2E_{\rm M}(k), \tag{3}$$

which is in the range $-1 \le r(k) \le 1$. This quantity characterizes the fractional magnetic helicity at each wavenumber. At early times, the scale where $r(k)$ is maximum is at somewhat smaller scales, reflecting perhaps the gradual separation of the initial bipoles of the emerging structure.

In is interesting to note that the two-dimensional magnetic energy spectra shown here do not possess a sub-inertial range, i.e., the spectrum for small k is approximately flat and not rising. This is a general feature of two-dimensional spectra that has also been seen in other spectra (to provide details, e.g., classes paper).

Table 1:

case	$\mathcal{E}_{\rm M}$	$\mathcal{H}_{\rm M}$	$\mathcal{H}_{\rm C}$	$L_{\rm M}$	$r_{\rm M}$
E-140	4.47	22.1	0.68	9.99	0.25
E-280	2.91	13.6	0.35	9.30	0.25
E-320	2.53	10.8	0.27	8.91	0.24
N-140	4.42	37.0	0.72	9.54	0.44
N-280	3.51	36.0	0.44	9.70	0.53
N-320	3.23	33.6	0.37	9.48	0.55

In both cases with and without eruption, the

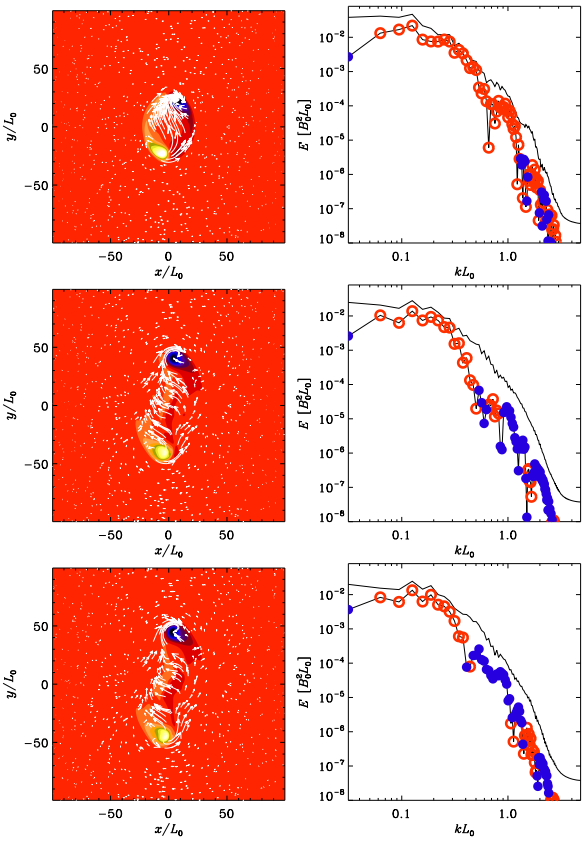

Figure 1: xy slice and spectra for the erupting case.

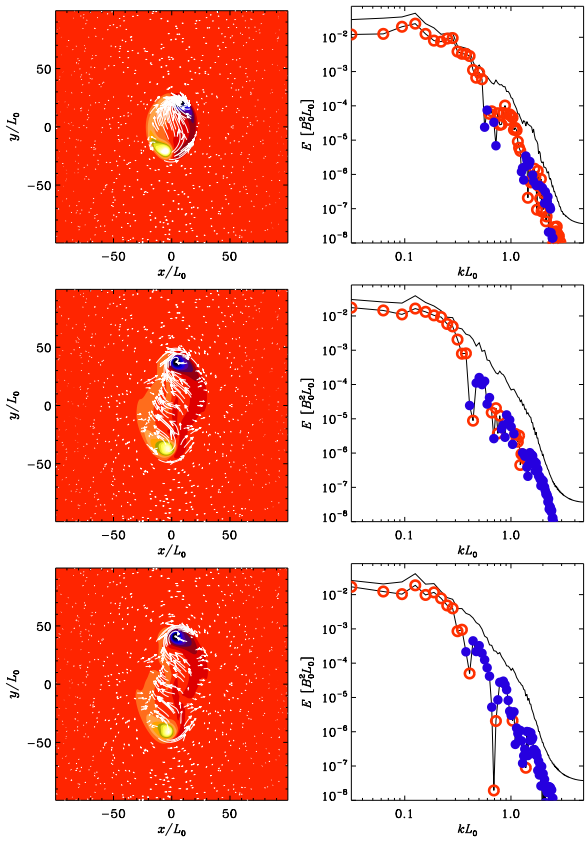

Figure 2: xy slice and spectra for nonerupting case.

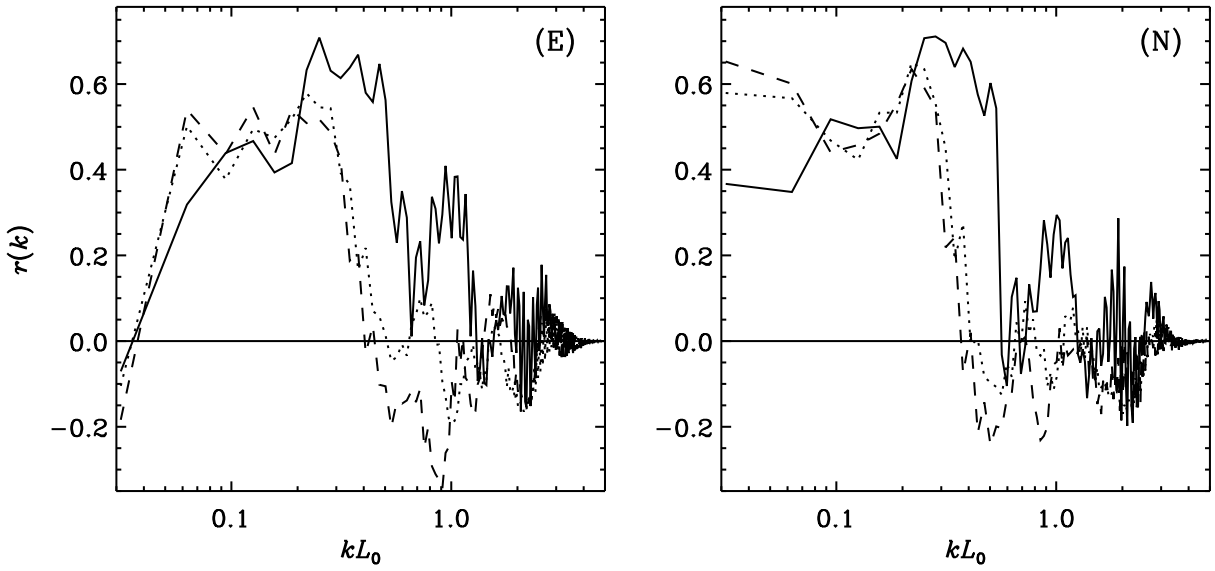

Figure 3: Fractional magnetic helicity spectra.

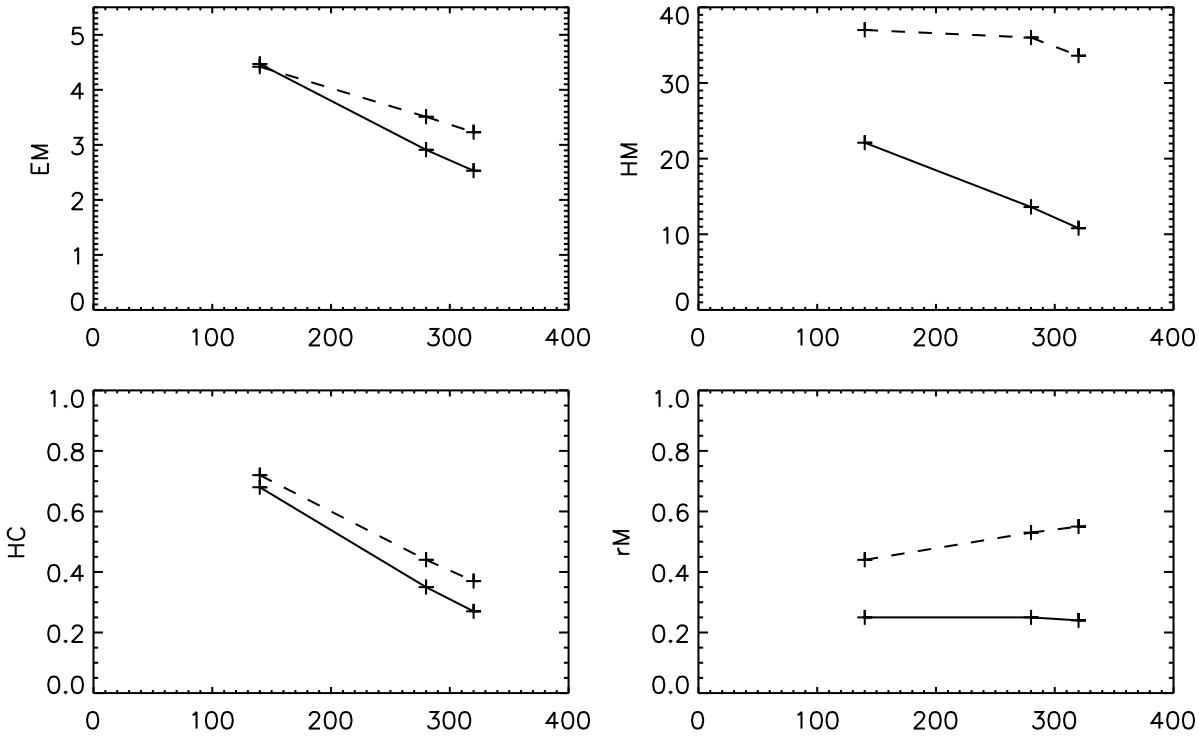

Figure 4: Time dependence.

magnetic energy density, the magnetic helicity density, the current helicity density, and the integral scale are monotonically decrease with time. However, the *fractional helicity evolves differently in the erupting and non-erupting cases*: it increases in the non-erupting case (from 0.44 to 0.55), but it decreases by a small amount (from 0.25 to 0.24) in the erupting case.

The initial values of magnetic energy are about similar in the two cases, but it drops faster in the erupting case. The magnetic helicity is, even at early times, weaker in the erupting case. This combination implies that the fractional magnetic helicity is about constant in the erupting case, but in-

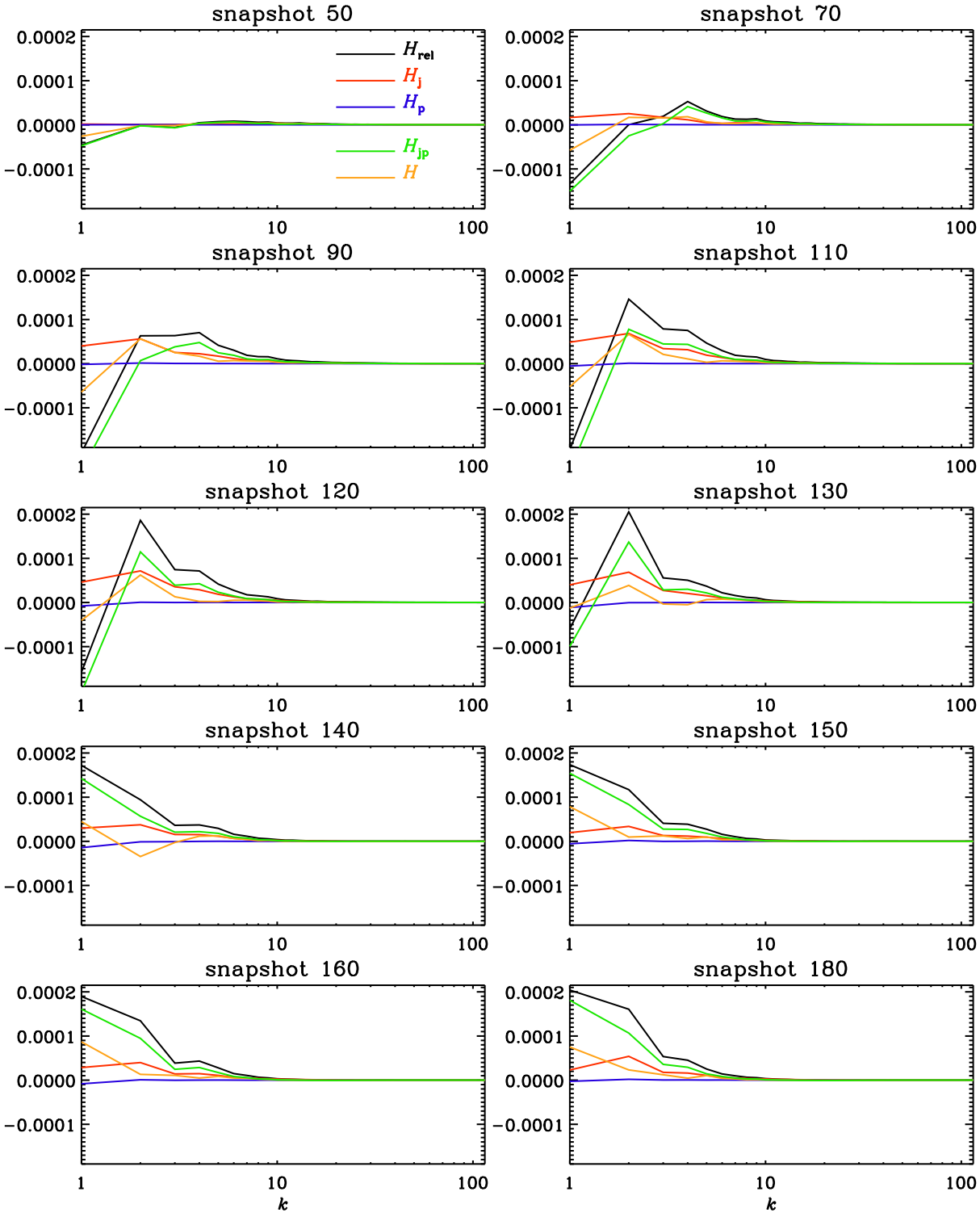

Figure 5: The different spectra for the full volume at the 10 times.

creasing in the non-erupting case. The correlation length, on the other hand, is nearly constant in the non-erupting case, but decreases by about 10% in the erupting case.

Decomposition into potential and current carrying parts

We now consider the decomposition of the magnetic field into potential and current carrying parts, i.e.,

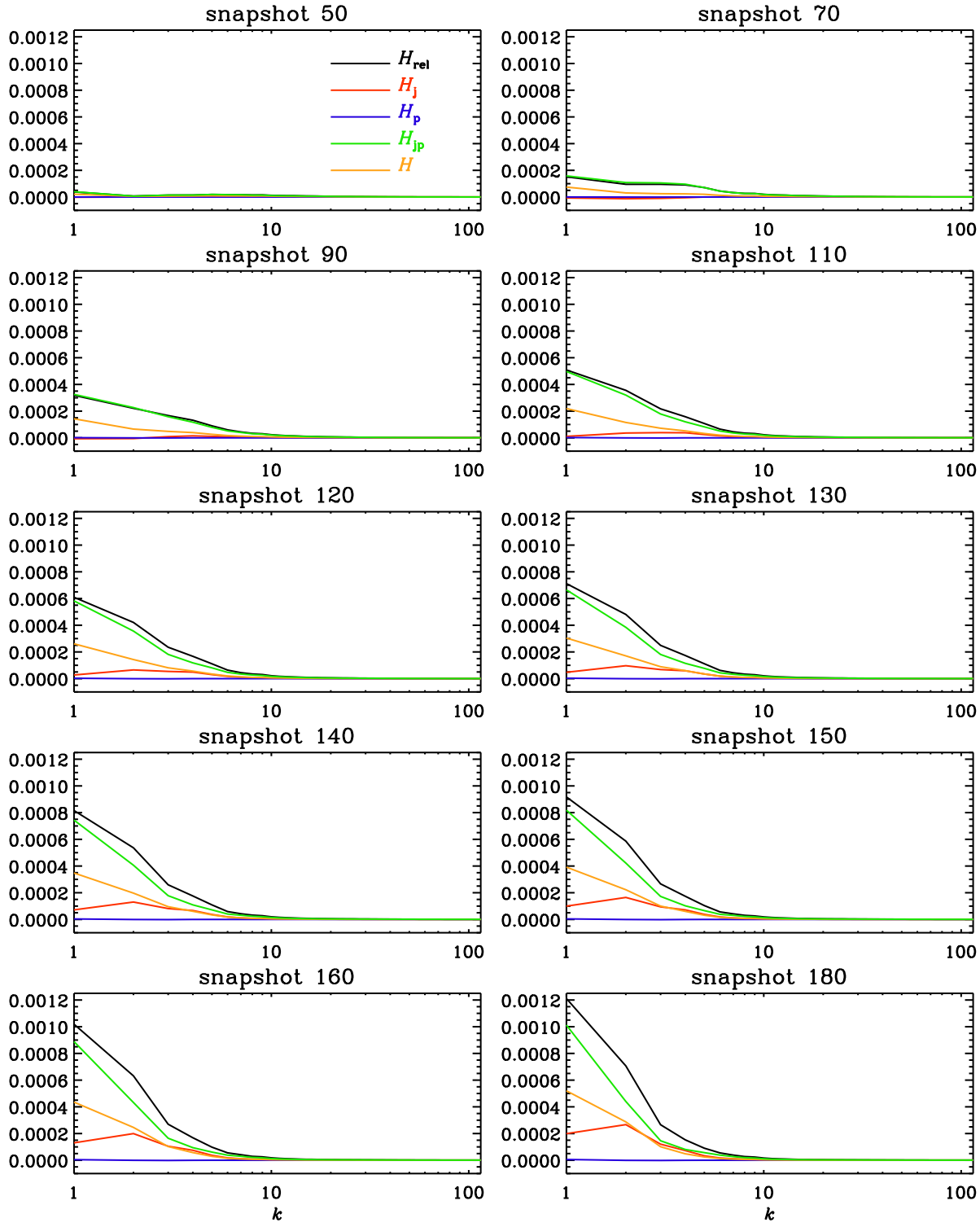

Figure 6: Same as Figure 5, but for the stable case.

we write

$$\boldsymbol{B} = \boldsymbol{B}_{\rm P} + \boldsymbol{B}_{\rm J}, \tag{4}$$

and compute the associated magnetic vector potential $\boldsymbol{A}$ in the DeVore gauge, i.e., $A_z = 0$, with

$$\boldsymbol{A} = \boldsymbol{A}_{\rm P} + \boldsymbol{A}_{\rm J}. \tag{5}$$

Note that, for computing the magnetic helicity, $\boldsymbol{A} \cdot \boldsymbol{B} = A_x B_x + A_y B_y$, so the B_z component of the field does not enter and all the information is in B_x and B_y alone. The relevant `IDL` routines are

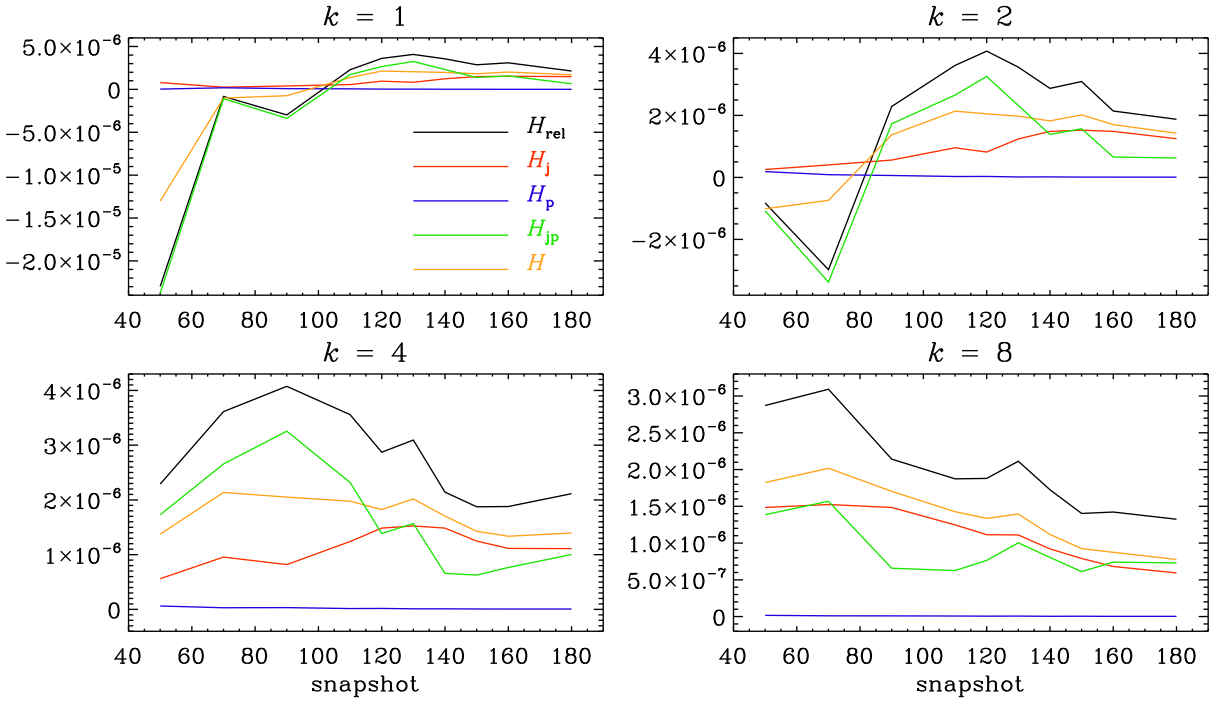

Figure 7: Time dependence of the different spectral helicities for the full volume.

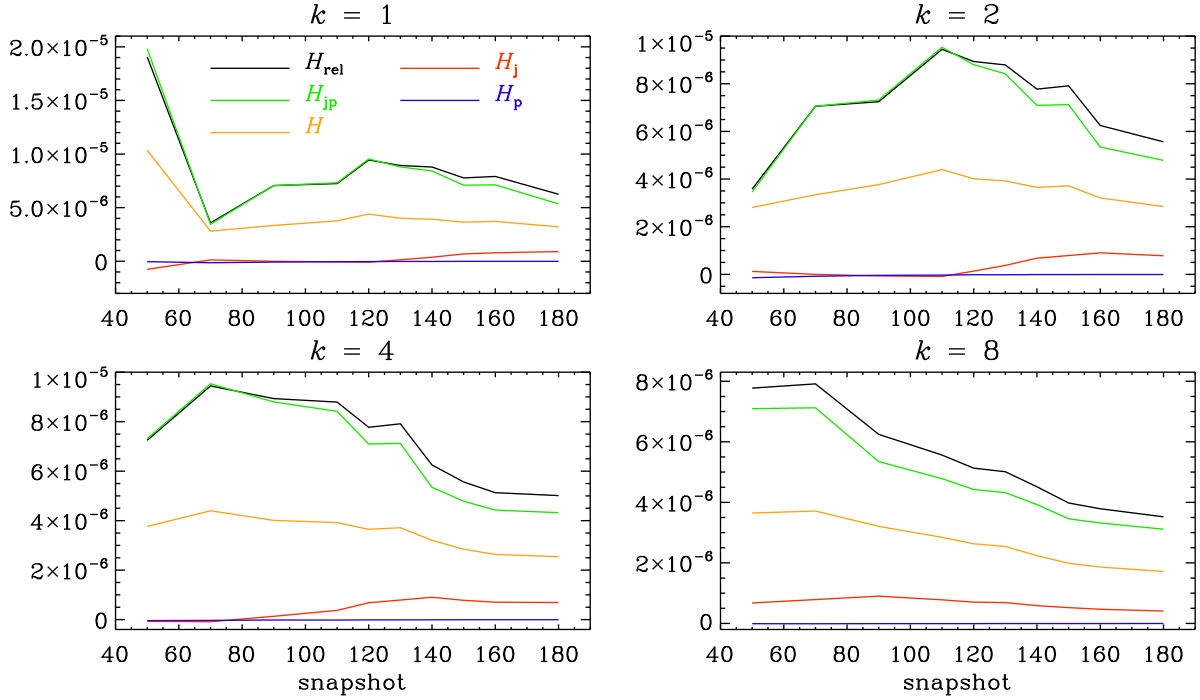

Figure 8: Same as Figure 7, but for the stable case.

publicly available[1]. We compute the magnetic helicity spectrum from the Fourier transforms[2] of vector potential and magnetic field, denoted by hat: $\hat{\boldsymbol{A}}(\boldsymbol{k})$ and $\hat{\boldsymbol{B}}(\boldsymbol{k})$,

$$H(k) = \tfrac{1}{2}\int_{4\pi} \hat{\boldsymbol{A}}\cdot\hat{\boldsymbol{B}}^*\,k^2\,\mathrm{d}\Omega + \mathrm{c.c.} \qquad (6)$$

[1] https://www.nordita.org/~brandenb/projects/issi19/etienne/

[2] The Fourier transforms for 311 points is slower than for 310 points, so I skipped the last point. This typically makes an 0.7% difference. OK, I can use 311 next time.

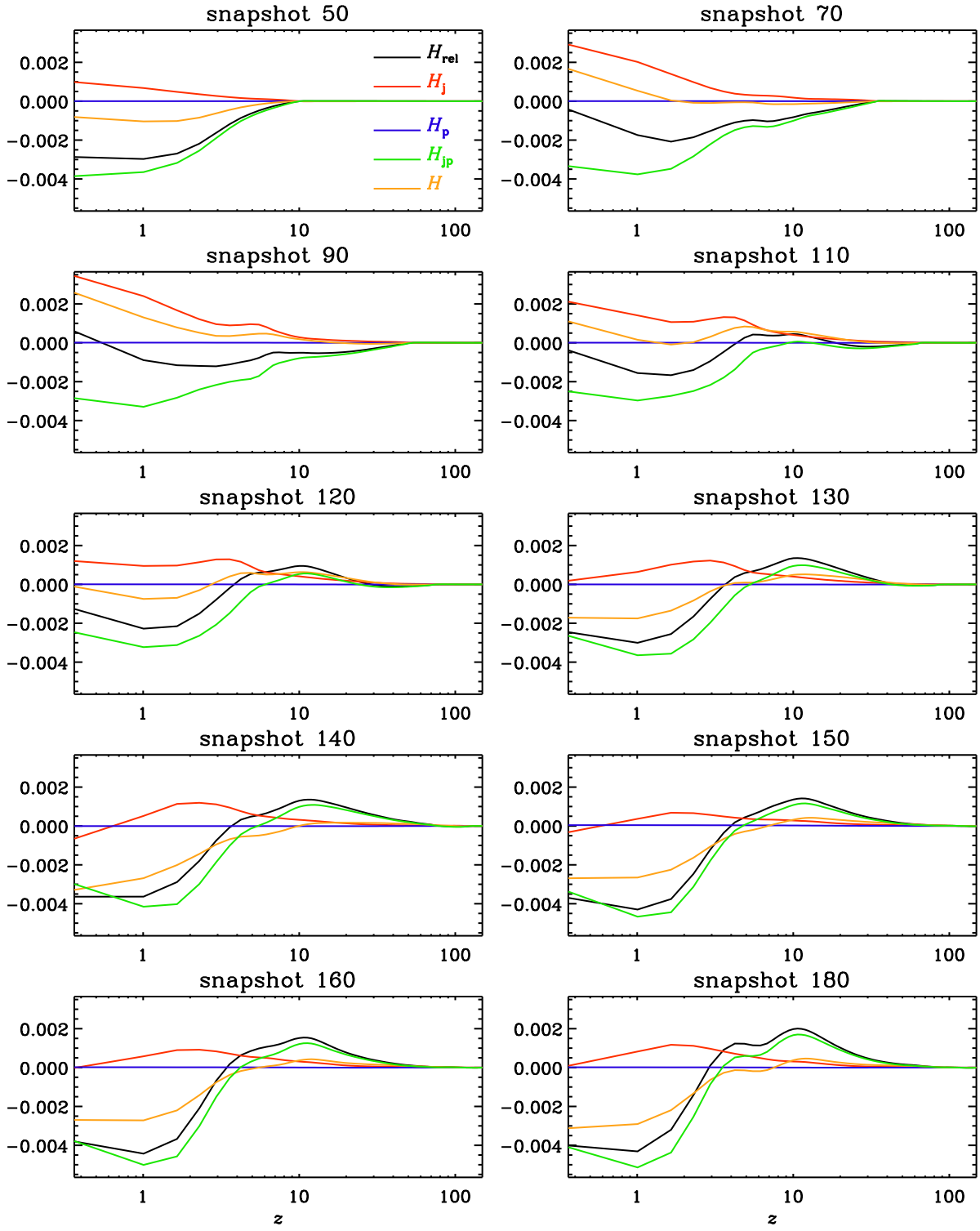

Figure 9: Horizontal spectral helicities for $k = 1$ versus z.

where the factor 1/2 accounts for the two contributions resulting from having added the complex conjugate (c.c.). Note that $\int H(k)\,\mathrm{d}k = \langle \boldsymbol{A}\cdot\boldsymbol{B}\rangle$ is the mean magnetic helicity density computed in real space.

We consider different combinations of potential and current carrying parts, in particular

$$H_{\rm P}(k) = \tfrac{1}{2}\int_{4\pi} \hat{\boldsymbol{A}}_{\rm P}\cdot\hat{\boldsymbol{B}}^*_{\rm P}\,k^2\,\mathrm{d}\Omega + \text{c.c.} \qquad (7)$$

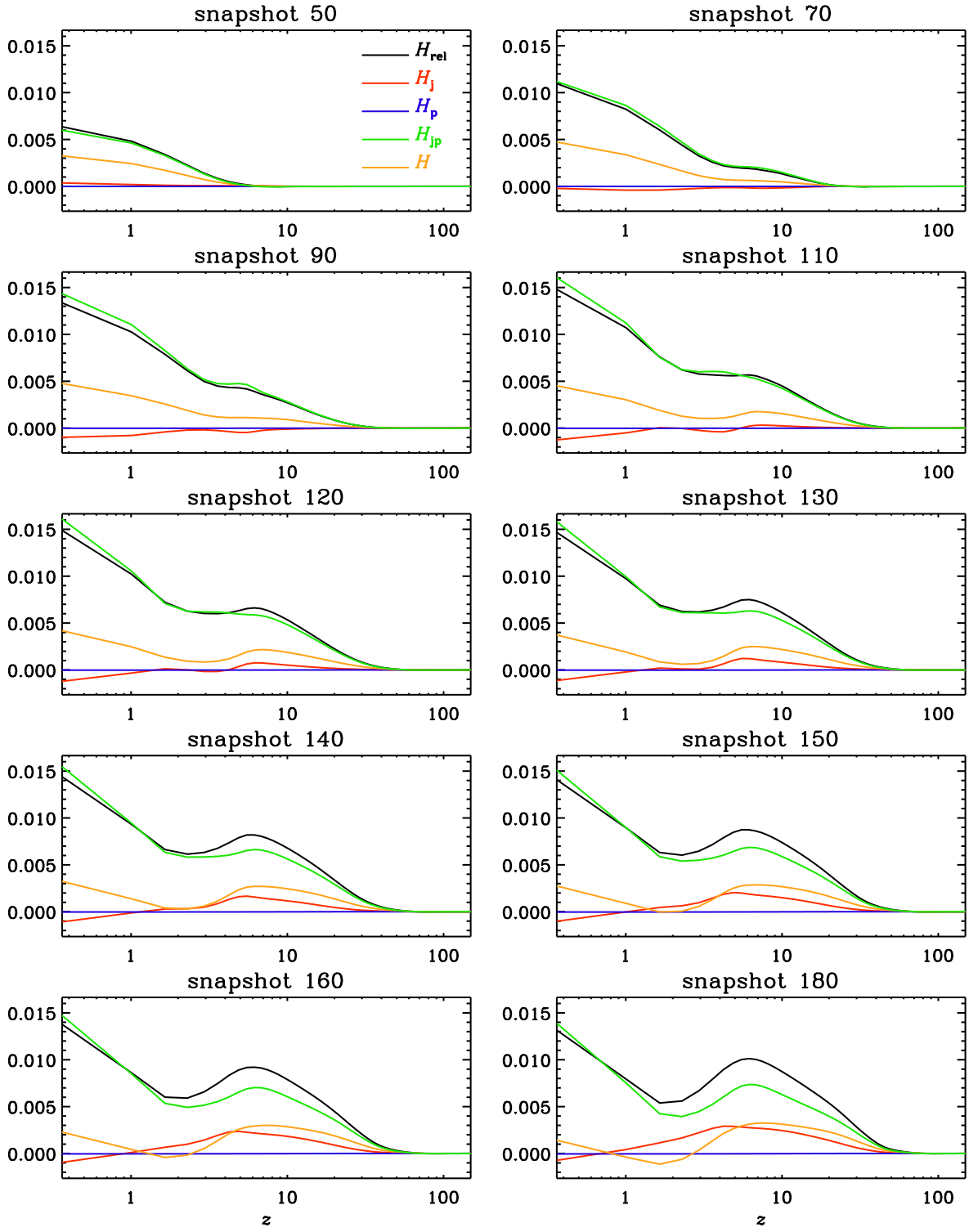

Figure 10: Same as Figure 9, but for the stable case.

and

$$H_{\rm J}(k) = \tfrac{1}{2}\int_{4\pi} \hat{\boldsymbol{A}}_{\rm J}\cdot\hat{\boldsymbol{B}}_{\rm J}^{*}\,k^2\,{\rm d}\Omega + {\rm c.c.}, \qquad (8)$$

respectively, and also the relative mean magnetic helicity density,

$$H_{\rm rel}(k) = \tfrac{1}{2}\int_{4\pi} \left(\hat{\boldsymbol{A}}+\hat{\boldsymbol{A}}_{\rm P}\right)\cdot\left(\hat{\boldsymbol{B}}-\hat{\boldsymbol{B}}_{\rm P}\right)^{*}\,k^2\,{\rm d}\Omega + {\rm c.c.}. \qquad (9)$$

Figure 5 shows that the relative spectral magnetic

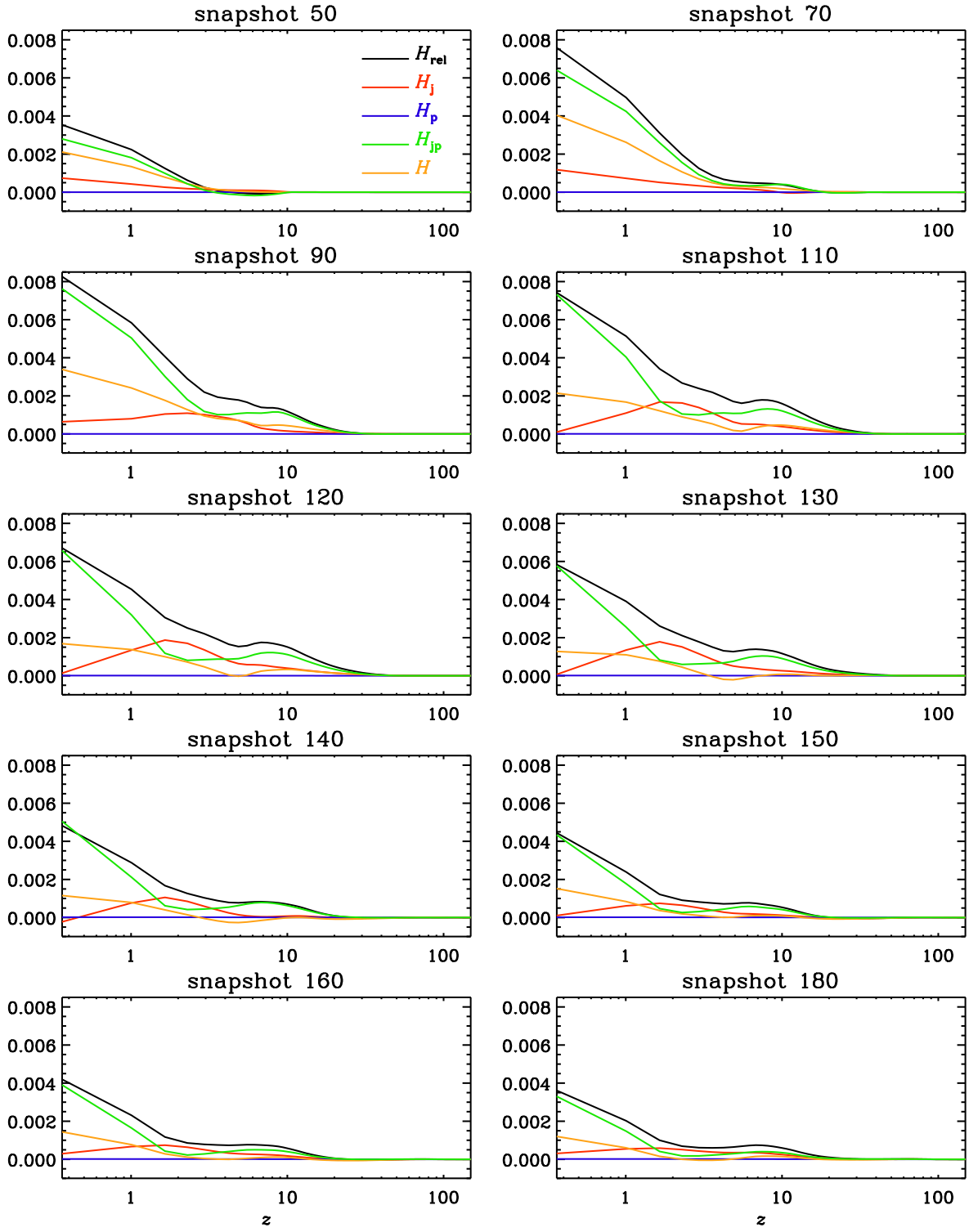

Figure 11: Same as Figure 9, but for $k = 2$.

helicity, $H_{\rm rel}(k)$, is governed by the contributions from small values of k (1 to 4). At $k > 2$, it is always positive, but at early times, it is negative at $k = 1$ and 2.

Comparing with the stable case (Figure 6), we see that now the spectral magnetic helicity is always positive, even at low k. It is also about 6 times bigger than in the unstable case. This suggests that the negative sign in the unstable case could be caused by the actual eruption.

The time evolution is shown in Figure 7, which shows the sign change at snapshot 110 for $k = 1$

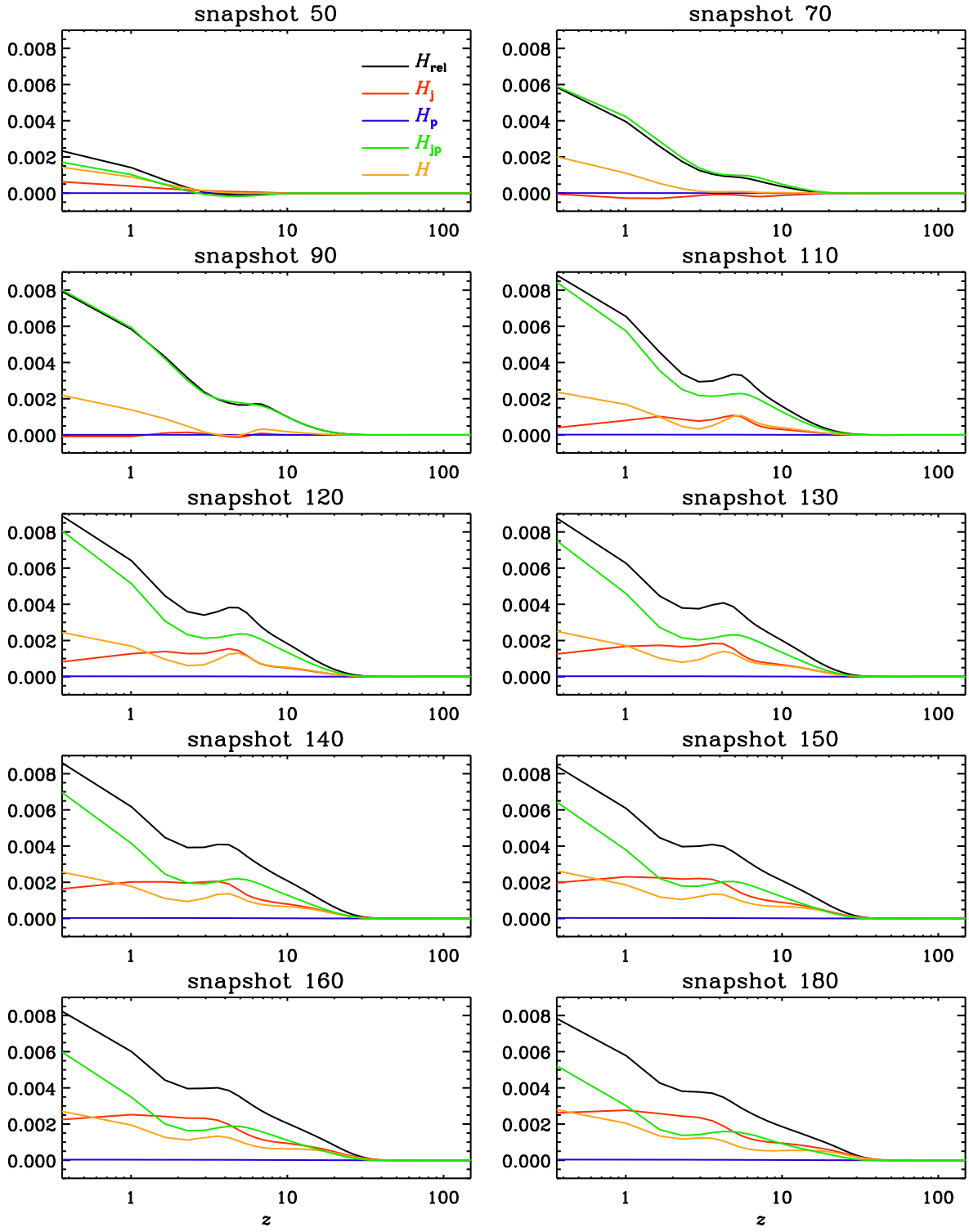

Figure 12: Same as Figure 11, but for the stable case.

and at snapshot 80 for $k = 2$. In the non-erupting case (Figure 8), the spectral magnetic helicity is, again, always positive. This is quite striking even at early times, where we see a mild decline from strong positive values in the beginning. At $k = 4$ and 8, the spectral magnetic helicity is similar to that in the erupting case, but it is now about 3 times smaller.

The evolution of $H_J(k)$ is rather different: it is mostly positive and growing for $k = 2$ and 4, but decaying for $k = 8$. $H_P(k)$ is in all cases basically vanishing. The behaviors of $H_{JP}(k)$ and $H(k)$ are

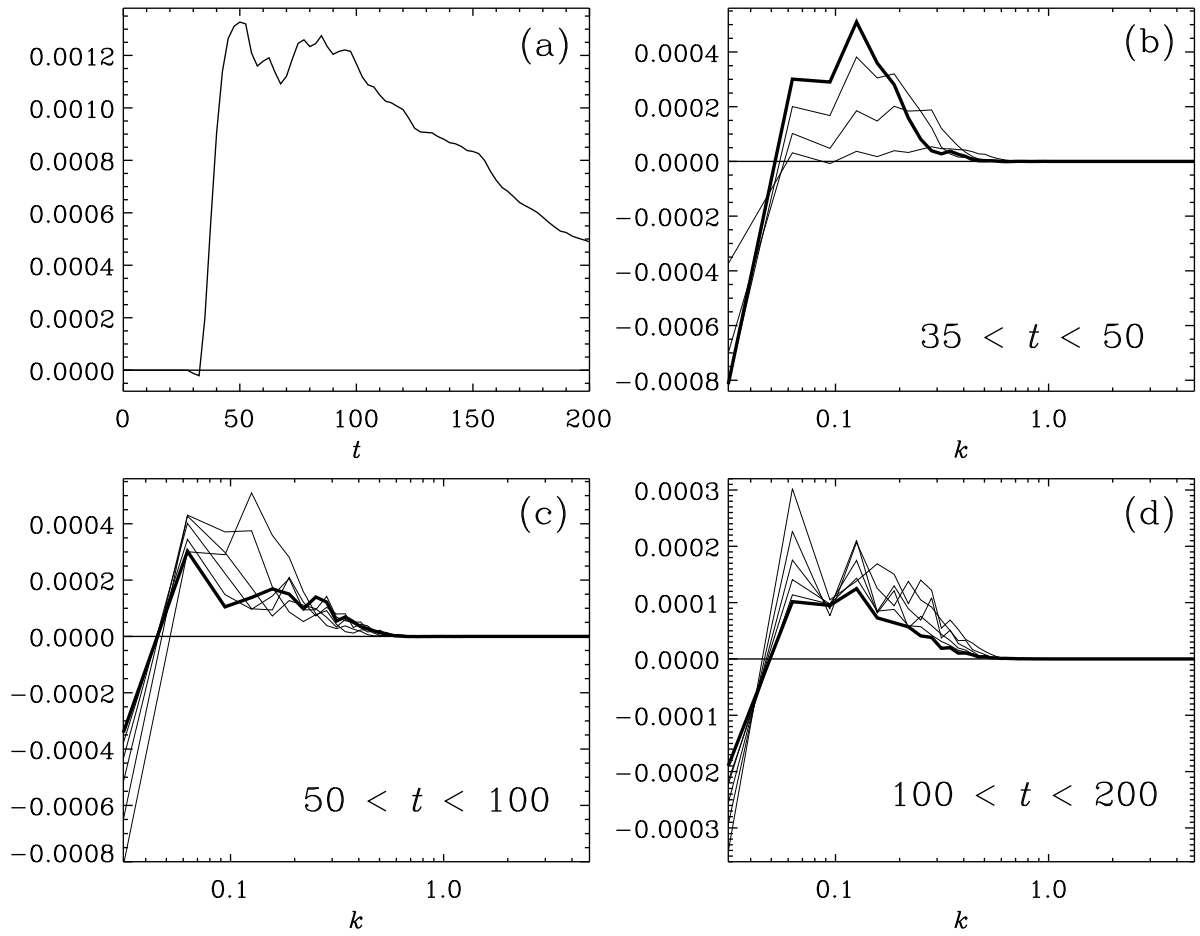

Figure 13: (a) mean magnetic helicity flux on the lower boundary ($z = z_1$) versus time; (b) spectral magnetic helicity flux versus k for early times; (c) spectral magnetic helicity flux versus k for intermediate times; (d) spectral magnetic helicity flux versus k for late times. In each of panels (b)–(d), the last time is shown as a fat line.

Table 2: Mean magnetic helicities for the different snapshots (k integrals over the full volume spectra).

snap	$H_{\rm rel}$	$H_{\rm J}$	H	$H_{\rm JP}$
50	0.00004	0.00005	0.00000	−0.00001
70	0.00011	0.00013	−0.00002	−0.00002
90	0.00020	0.00024	−0.00001	−0.00004
110	0.00030	0.00028	−0.00003	0.00001
120	0.00033	0.00027	−0.00005	0.00006
130	0.00037	0.00022	−0.00005	0.00014
140	0.00040	0.00014	−0.00000	0.00026
150	0.00042	0.00011	0.00014	0.00031
160	0.00045	0.00014	0.00015	0.00031
180	0.00049	0.00015	0.00013	0.00034

broadly similar to those of $H_{\rm rel}(k)$, which are rather different from those of $H_{\rm J}(k)$.

Table 3: Same as Table 2, but for the stable case.

snap	$H_{\rm rel}$	$H_{\rm J}$	H	$H_{\rm JP}$
50	0.00036	0.00002	0.00020	0.00034
70	0.00093	−0.00002	0.00039	0.00095
90	0.00141	0.00005	0.00058	0.00135
110	0.00182	0.00021	0.00078	0.00161
120	0.00200	0.00030	0.00087	0.00171
130	0.00217	0.00038	0.00095	0.00179
140	0.00232	0.00046	0.00103	0.00186
150	0.00245	0.00055	0.00110	0.00191
160	0.00258	0.00062	0.00117	0.00195
180	0.00279	0.00077	0.00128	0.00202

Height dependence of spectral helicities

Next, we compute the various spectral mean relative magnetic helicities in two-dimensional horizon-

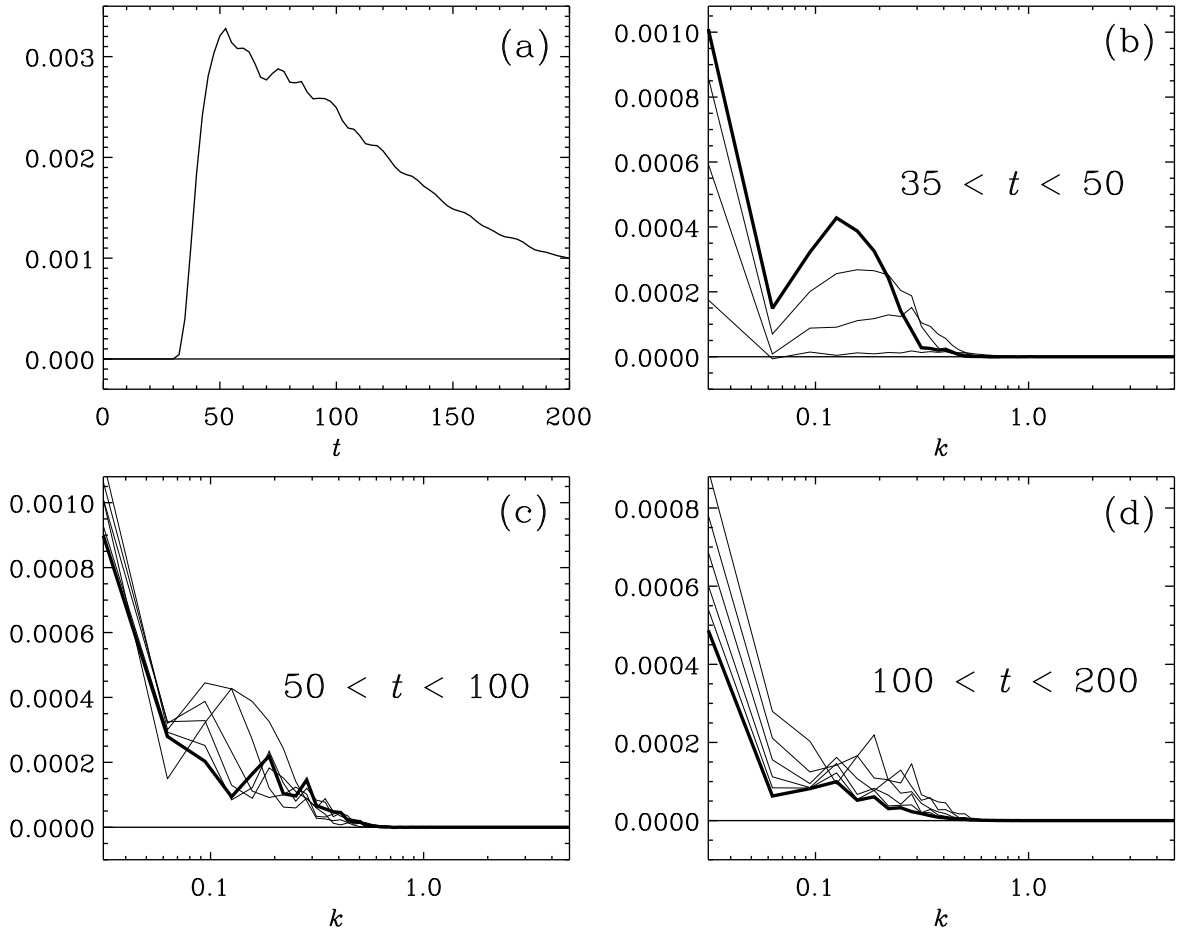

Figure 14: Same as Figure 13, but for the stable case.

tal slices. The vertical *average* over the k integrals of these spectra agrees with k integrals of the volume spectra. Those values are listed in Table 2. In Figure 9 we show the z dependence at the 10 times for $k = 1$ and in Figure 11 for $k = 2$.

Interestingly, we find a height reversal of the spectral magnetic helicity at $z \approx 4$ for $k = 1$. This sign reversal is not seen in $H_J(k)$, which stays mostly positive.

In the stable case, no sign reversal is seen; see Figure 10. However, both for $k = 1$ and for $k = 2$ (Figure 12), there is a local positive maximum at $z = 5$, which is similar to the erupting case. The main difference between stable and unstable cases is that the spectral magnetic helicity is negative at the bottom in the unstable case, but not in the stable case. This is true also at later times. The values of the various helicities for the stable case are listed in Table 3.

Spectral magnetic helicity flux

We compute the spectral magnetic helicity flux on the lower boundary as

$$F(k) = \int (\tilde{\boldsymbol{E}} \times \tilde{\boldsymbol{A}}^*_{\rm P})_z \, k^2 {\rm d}\Omega + {\rm c.c.}, \qquad (10)$$

where $\tilde{\boldsymbol{E}}$ and $\tilde{\boldsymbol{A}}_{\rm P}$ are the Fourier transforms of the electric field $\boldsymbol{E} = -\boldsymbol{u} \times \boldsymbol{B}$ and the vector potential of the reference field on the boundary, $\boldsymbol{A}_{\rm P} = \boldsymbol{\nabla}_\perp \times (\psi \hat{\boldsymbol{z}})$, respectively. Here $\boldsymbol{\nabla}^2_\perp \psi = -B_z$ on the lower boundary $z = z_1$. Thus, in Fourier space, we compute $\tilde{A}_{{\rm P}\,x} = {\rm i}k_y \tilde{B}_z/k^2$ and $\tilde{A}_{{\rm P}\,y} = -{\rm i}k_x \tilde{B}_z/k^2$.

The integral over $F(k)$ gives $\int F(k)\,{\rm d}k = 2\langle \boldsymbol{E} \times \boldsymbol{A}_{\rm P} \rangle_z$. To get the flux across the boundary, we would still need to multiply by the surface area.

References

Leake, J. E., Linton, M. G., & Antiochos, S. K., "Simulations of emerging magnetic flux. II. The formation of unstable coronal flux ropes and the

initiation of coronal mass ejections," *Astrophys. J.* **787**, 46 (2014).